JOM, Vol. 75, No. 12, 2023
https://doi.org/10.1007/s11837-023-06141-6

TECHNICAL ARTICLE

Formation, Aggregation, and Composite with Oxide Mechanisms of Oxysulfide in 1215MS Free-Cutting Steel

QIANREN TIAN,[1] WEI SHEN,[1] XIAOYU ZHANG,[1] BIN LIU,[1,2] XIANGYU XU,[1] and JIANXUN FU[1,3]

1.—Center for Advanced Solidification Technology (CAST), State Key Laboratory of Advanced Special Steel, Shanghai University, Shanghai 200444, People's Republic of China. 2.—Ansteel Beijing Research Institute Co., Ltd, Beijing Future Science Park, Beijing 102211, People's Republic of China. 3.—e-mail: fujianxun@shu.edu.cn

Oxygen is an important element for improving the sulfide morphology in steels that require machinability. Therefore, 50 ppm oxygen was added to 1215MS free-cutting steel under industrial conditions; the effect of oxygen on sulfide morphology and the formation mechanism of three types of sulfides were explored. The precipitation temperature of sulfide in steel at equilibrium state is 1489.98°C; oxygen can dissolve in MnS to form spherical single-particle Mn(S,O). Annular polycrystalline Mn(S,O) with a diameter of 10 μm was observed by characterization of scanning electron microscopy and electron backscatter diffraction (SEM and EBSD). It is formed by three stages of contact, sintering and densification. Sintering force is a vital force in the formation of polycrystalline Mn(S,O). Mn(S,O)-$MO_{x(M = Si,Al,Mn,Fe)}$ composite inclusion is formed by a liquid inclusion, $(Mn,Si,Al,Fe)_x(O,S)_y$; the precipitation order of different phases is FeO, Mn(S,O), $(Si,Mn,Al)_xO_y$ and $(Si,Al,Mn)_xO_y$. $(Si,Mn,Al)_xO_y$ is Mn_2SiO_4 with dissolved Al, while $(Si,Al,Mn)_xO_y$ is $Mn_3Al_2Si_3O_{12}$ when the atomic content of Al_2O_3 in liquid inclusion is > 0.063.

INTRODUCTION

Manganese sulfide (MnS) inclusion is one kind of common free-cutting phases in steel, and well-shaped MnS can avoid causing anisotropy to the mechanical properties of steel.[1–3] Therefore, controlling the morphology of sulfides has become the key to improving the processing performance of steel.[4,5]

Retaining a certain amount of oxygen in steel can promote the spheroidization of sulfides, enhance their fracture degree during the cutting process and thus improve the cutting performance of the steel.[6] With increasing of oxygen content in steel, the morphology of sulfide changes from angular (type III) to dendritic or clustered (type II) and spherical (type I); the classification of morphology of sulfide was first proposed by Sims.[7] Oxygen is considered a super-monotectic stabilizer, which can significantly stabilize the monotectic structure of sulfide, while C and Si are strongly eutectic elements for the formation of sulfide.[8] In addition, the relationship of oxide and sulfide is also an important research focus on the influence of oxygen on sulfides.

In the MnO-SiO2-Al_2O_3-MnS system, the solubility of MnS is strongly influenced by the Al_2O_3 content and MnO/SiO_2 ratio.[9] When the Al_2O_3 content is constant, the solubility increases with the increase of MnO/SiO_2 ratio. When the MnO/SiO_2 ratio is constant, the solubility decreases with the increase of Al_2O_3 content; based on the Al_2O_3 content and MnO/SiO_2 ratio, the liquid phase may be saturated not only by MnS but also by other solid oxide phases. Considering the utilization of inclusions in free-cutting steel, reducing the Al_2O_3 content and increasing the MnO/SiO_2 ratio may be beneficial. Kim et al.[10] suggested that the activity coefficient of MnO decreases with the increase of the mole fraction ratio of SiO_2/(MnO-SiO_2) (abbreviated as $S/MS_{at.\%}$). Al_2O_3 and MnS have no obvious effect on the activity coefficient of MnO. On the other hand, the activity coefficient of MnS strongly

(Received April 28, 2023; accepted September 5, 2023; published online September 26, 2023)

depends on $S/MS_{at.\%}$, which first increases with the increase of $S/MS_{at.\%}$ and decreases at high $S/MS_{at.\%}$ concentration. Increasing the content of Al_2O_3 in MnO-SiO2-Al_2O_3-MnS system will also increase the activity coefficient of MnS. Wang et al.[11] observed the two-dimensional (2D) and three-dimensional (3D) morphology of Al_2O_3-MnO-SiO_2(-MnS) composite inclusion and analyzed the importance of SiO_2 in the formation of composite inclusions. The composite liquid inclusion is formed by the reaction of SiO_2 core with Mn and Al, and then MnS nucleates and precipitates on the composite inclusions. Zhang et al.[12] believed that MnS precipitates from liquid inclusion $(Mn,Si)_x(O,S)_y$ in free-cutting steel with oxygen content exceeding 0.0125 wt.%; sulfide precipitates after oxide has precipitated. Ren and Zhang[13] indicated that in 304 stainless steels with Al content $< 0.001\%$, liquid inclusions rich in SiO_2-MnO hardly affect the precipitation of MnS inclusions. With the increase of Al in the steel, more solid inclusions rich in Al_2O_3 are formed, which can serve as nucleation points for MnS inclusions and significantly promote the precipitation of MnS inclusions during the cooling process of steel.

Our previous research[14] elucidated the effect of oxygen activity on the precipitation of MnS in the MnO-SiO_2-MnS system and summarized the precipitation mechanism of MnO-SiO_2-MnS composite inclusion in 1215MS free-cutting steel. However, more forms of liquid inclusions have been found in 1215MS free-cutting steel, indicating that the formation mechanism of different morphologies of inclusions still needs to be further studied. Therefore, 50 ppm total oxygen content was added into 1215MS free-cutting steel, and three different morphologies of oxysulfide were observed using the scanning electron microscopy (SEM) with energy-dispersive spectrometry (EDS) and electron backscatter diffraction (EBSD). Their formation and evolution mechanisms were analyzed based on their 2D and 3D morphologies.

EXPERIMENTAL

Industrial Practice

The 1215MS free-cutting steel samples were obtained at the position of half distance to the center of length and width from the industrial bloom with a section size of 425 mm × 320 mm. The smelting process of the steel mainly goes through basic oxygen furnace (BOF)-ladle furnace (LF)-continuous casting (CC). In the refining process, the deoxidizers used are mainly strong deoxidizer aluminum and weak deoxidizer ferrosilicon, which were added to the steel in the refining process.

Chemical Composition

The contents of metal elements and phosphorus were detected by a direct-reading spectrometer (Model: Spectro, SPECTROMAXx). Carbon and sulfur in the steel were detected by a carbon sulfur analyzer (model: NCS, CS-2800). An oxygen and nitrogen determinator were employed to detect the total oxygen content (model: LECO, ON-736).

Inclusion Characterization

In this study, 2D morphology of the inclusions was observed to study the compositional relationships between sulfides and oxides within the composite inclusions, and it is essential for the analysis of the precipitation order of sulfides and oxides. Electrolytic etching was used to obtain the complete 3D morphology of inclusions in the steel, and the electrolytic solution used is neutral, which is non-destructive to the morphology of the inclusions. The solution contains 1% tetramethylammonium chloride, 10% acetylacetone and 89% methanol. The microstructure of specimens was observed by SEM, and their compositions were analyzed (in atomic percent, at.%) using SEM-EDS. EBSD was used to analyze the orientation relationships of particles in polycrystalline inclusion, and the corresponding results were analyzed using the HKL Channel 5 software.

FORMATION MECHANISMS OF DIFFERENT TYPES OF SULFIDES

Single-Particle Oxysulfide

The test results of chemical composition of 1215MS free-cutting steel are shown in Table I. The content of C, Si, Mn, P, S, acid soluble aluminum (Als) and total oxygen content $O_{[T]}$ are 0.06 wt.%, 0.04 wt.%, 1.27 wt.%, 0.05 wt.%, 0.36 wt.%, 0.0051 wt.% and 0.0050 wt.%, respectively. The content of Si, Mn, Al and O may lead to the formation of oxides.

The phase diagram module in Factsage 7.3 (with the database of FactPS, FToxid and FSstel) was used to calculate the relationship between the microstructure and sulfide content of 1215MS steel with 50 ppm oxygen and the temperature, as shown in Fig. 1. The liquidus and solidus temperatures of the steel are 1512.92°C and 1458.79°C, respectively. MnS starts to precipitate at 1489.98°C, and its content increases rapidly in the mushy zone where the δ-Fe (BCC-Fe) content exceeds 50%. Although MnS precipitates most in the mushy zone, it precipitates in small amounts after the liquid steel is fully solidified, with a final mass percentage of MnS of 0.98 wt.% in γ-Fe (FCC-Fe).

Oxygen is an important element affecting the morphology of sulfide, which mainly forms oxysulfide with MnS in the presence of sufficient oxygen in Fe-Mn-S-O system.[15] Based on the liquidus and solidus temperatures of steel and the precipitation temperature of MnS, the formation pattern of phases precipitated by Mn and S under 50 ppm oxygen content at the temperature of 1450–1550°C was also calculated by the phase diagram module of

Table I. Chemical compositions of 1215MS free-cutting steel (in mass percent, wt.%)

Composition	C	Si	Mn	P	S	Als	$O_{[T]}$
Content	0.06	0.04	1.27	0.05	0.36	0.0051	0.0050

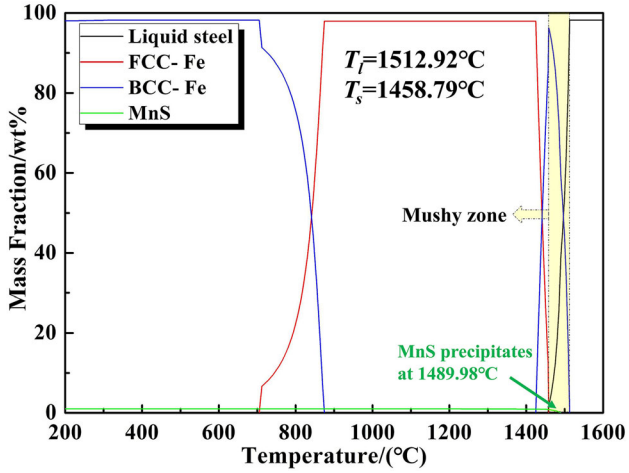

Fig. 1. Relationship between the microstructure and sulfide content of 1215MS steel with 50 ppm oxygen content and the temperature.

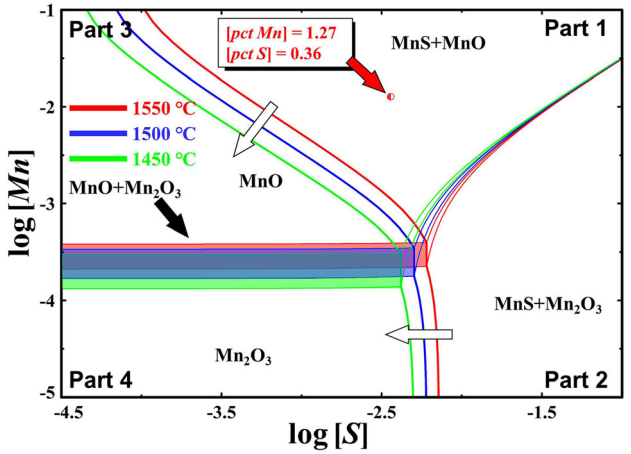

Fig. 2. Variation pattern of the phase formed by Mn and S in 1215MS free-cutting steel containing 50 ppm oxygen content in a temperature of 1450–1550°C (Color figure online).

Factsage 7.3, as shown in Fig. 2. The phases can be divided into four regions according to the different Mn and S contents: part 1, when both Mn and sulfur are high, the phase composition is MnS and MnO, i.e., Mn(S,O) or MnS-MnO composite inclusion; part 2, when Mn is low and S is high, the phase composition is MnS + Mn_2O_3; part 3, when Mn is high and S is low, the phase composition is MnO; part 4, when Mn and S are both low, the composition of the phase is Mn_2O_3. There is a transition region between part 3 and part 4, as shown by the shadow area and black arrow in the figure; the composition of the phase is MnO + Mn_2O_3. At the point of 1.27 wt.% Mn and 0.36 wt.% S, it is in part 1, with the phase becoming Mn(S,O), as shown by the red arrow in the figure. As temperature decreases (shown as white arrows), the sulfur-bearing region expands (the right side part of the thick lines), which means the content of Mn(S,O) is constantly enriched in steel, and Mn(S,O) is the final phase of oxysulfide in an equilibrium state.

The single sulfide particles were observed by SEM. The results showed that the morphology of sulfide is spherical or ellipsoidal (Fig. 3). The EDS result suggests that there is approximately 19 at.% oxygen content in sulfide, which means the sulfide particle is oxysulfide, i.e., Mn(S,O). The melting point of oxysulfide is related to the Mn content in steel. The higher the Mn content in steel, the higher the melting point of the oxysulfide is. The melting point of oxysulfide is within 900–1200°C.[16] Therefore, when the atomic content of Mn is approximately 30 at.%, the corresponding mass content is approximately 44 wt.%, and the melting point of the oxysulfide is approximately 1188°C, which means the oxysulfide here is the liquid phase after steel completely solidified.

Polycrystalline Oxysulfide

There is a class of oxysulfide with iron in its center and looks like an island in oxysulfide; the size of it is approximately 10 μm, as shown in Fig. 4. It is named after as annular polycrystalline Mn(S,O) inclusion. Annular Mn(S,O) inclusions have a larger ellipsoidal eccentricity than globular inclusion. The eccentricity of the annular Mn(S,O) inclusions, e, can be expressed as:

$$e = \frac{\sqrt{a^2 - b^2}}{a} \quad (1)$$

where a and b denote the long and short semi-axes of the ellipsoid, respectively, μm. Based on the SEM observations, the average values of a and b are 5 μm and 3 μm, respectively; therefore, e is 0.8 for the inclusion in Fig. 4a. The observation of the 3D morphology of such inclusions shows that Fe in annular Mn(S,O) forms a cavity after electrolysis, as shown in Fig. 4b, which means that Fe is not completely wrapped by Mn(S,O) but penetrates through Mn(S,O), which is also different from the formation mechanism of MnO-Mn(S,O), i.e., Fe is not the nucleation core of MnS.

The EBSD orientation analysis of annular Mn(S,O) shows that Mn(S,O) is actually composed of multiple grains, as shown in Fig. 4c and d, i.e., the combination of multiple grains forms annular

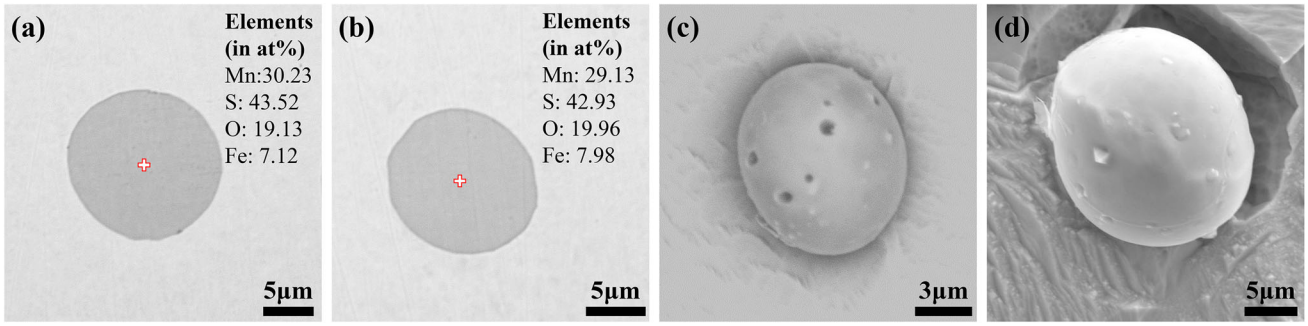

Fig. 3. Single-particle oxysulfide in 1215MS free-cutting steel: (a)–(b) 2D morphology; (c)–(d) 3D morphology.

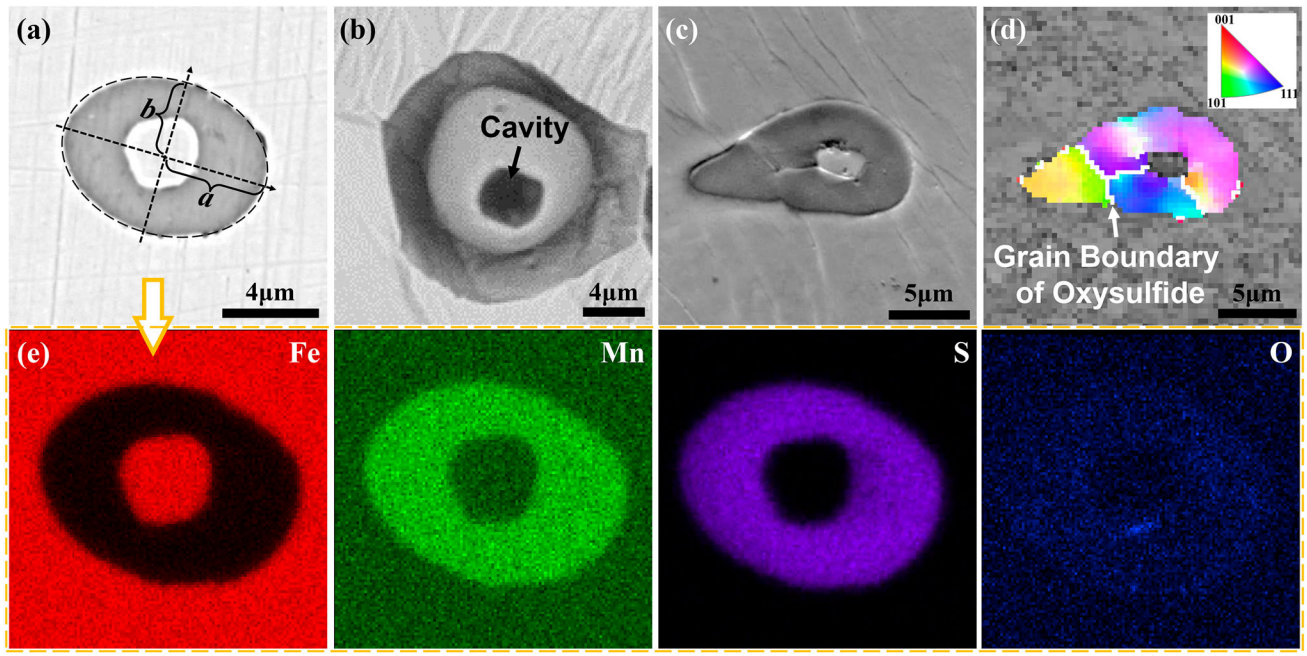

Fig. 4. Annular oxysulfide inclusion: (a) 2D morphology; (b) 3D morphology; (c) and (d) annular oxysulfide inclusion with EBSD result; (e) corresponding EDS element mapping for inclusion in (a).

Mn(S,O) particles. The grain boundaries of Mn(S,O) are shown as white lines between particles in Fig. 4d. According to the thermodynamics analysis of oxysulfide in "Single-Particle Oxysulfide" section, the precipitation process of sulfide is mainly in mushy zone, and inclusions still have a good tendency to move within the semi-liquid steel, especially when the nuclei are close to each other, and the natural growth of inclusions or mutual attraction between each other can lead to inter-particle aggregation. Aggregation forces between inclusion particles in steel can be cavity bridge forces;[17] van der Waals forces[18] and capillary forces at the steel surface have likewise been investigated.[19,20] Sudre and Lange[21] concluded that the intergranular aggregation is constituted by the viscous sintering between the particles under certain temperature and flow conditions, and the particles are bound to each other by the sintering forces formed by the surface diffusion of elements, grain boundary diffusion and bulk diffusion to each other. After connecting, the particles will be further sintered and densified by elemental diffusion, and the sintering and densification processes gradually transform multi-particles aggregates into individual particles. Caillet and Harrison[22] suggested that the sintering and coalescence process of particles will go through three stages: the initial stage, in which the diffusion of elements on the particle surface changes after the particles contact each other; in the intermediate stage, the diffusion of elements on the inclusion surface becomes the driving force of the sintering process and increases the neck dihedral angle (ψ) between inclusions, and the shrinkage cavity inside the inclusion particles will also change to the shape of low chemical potential; in final stage, the multi-particle aggregated inclusions evolute to the equilibrium morphology with the inner and outer surfaces reaching the minimum surface chemical potential.

Since the sulfide is precipitated in the mushy zone, the flow of the steel continues during the

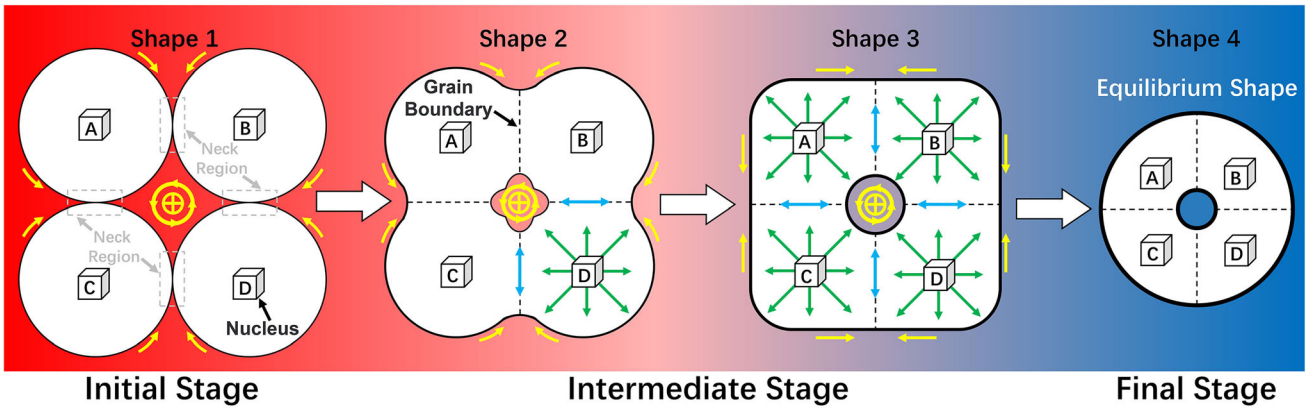

Fig. 5. Schematic diagram of the sintering and evolution process of four particles; yellow, blue and green arrows indicate surface diffusion, grain boundary diffusion and bulk diffusion, respectively (Color figure online).

growth of the sulfide. One situation that should be considered here is that when aggregation between particles occurs in the mushy zone, the intermediate void areas are filled by liquid steel, forming annular Mn(S,O), as shown in Fig. 4. A schematic diagram of the evolution of annular Mn(S,O) particles in steel are shown in Fig. 5 (with four particles in an ideal state as an example). The mutual contact of the oxysulfides is considered to be the initial stage of the agglomeration process. A neck is formed at the contact part; the elements diffuse mainly on the surface of the particles along the surface towards the neck region (as shown by the yellow arrows); the voids formed between the particles are filled by liquid steel, while the elements in liquid steel likewise diffuse towards the neck. As the temperature decreases, the elements continue to diffuse to the neck. The radius of grain boundaries formed between the particles expands, the neck curvature decreases, and the influence of grain boundary diffusion and bulk diffusion on the morphology increases (as shown by the blue and green arrows), forming the shape of the intermediate stage. When the location of the neck forms a plane as shape 3, the chemical potential at planes is lower than the convex arc region, so the elements in the convex arc region still diffuse to the neck region to reach the lowest surface energy of the shape as a whole. The void volume gradually decreases under the multiple element diffusion mechanism within particles and steel. Eventually, when the lowest surface energy is reached on the particle's inner and outer surfaces, a particle with a rounded shape is formed.

The outer shape of Mn(S,O) steel is not a spherical shape, but an ellipsoidal shape, which is related to the number and distribution of grain nucleus of particles. Based on the annular Mn(S,O) particles observed by EBSD, the sintering force, F^s, was analyzed, which can be defined as:[23,24]

$$F^s = \gamma_{PL}\kappa_{neck}A_{GB} + \gamma_{PL}l_{GB}\sin(\psi/2) \quad (2)$$

where κ_{neck} indicates the curvature of the neck region; it can be expressed as:

$$\kappa_{neck} = -2/r_P \quad (3)$$

r_P is the particle radius, μm; A_{GB} is the area of the grain boundary of the intergranular sintering part, $A_{GB} = \pi r_{GB}^2$, μm^2; r_{GB} is the radius of the grain boundary of the sintering neck, μm; l_{GB} is the outer circumference of the grain boundary of the intergranular sintering part, $l_{GB} = 2\pi r_{GB}$, μm; the observed ψ according to SEM observation result is usually $> 90°$. Therefore, the dihedral angles, ψ, here take the values of 135° and 180°.

The relationship between the sintering force and the particle and neck radius is shown in Fig. 6. The results show that while the sintering force increases with increasing particle size for the same neck radius, the sintering force increases and then decreases with the neck radius for the same particle radius, but the neck radius does not produce sintering force until it is not greater than the particle radius; the ratio of the neck radius to the particle radius is greater for increasing dihedral angle compared to 135°, and the range in which sintering force can be produced is greater. The two types of particles observed in the steel are shown in the 3D morphologies in Fig. 6. The relationship between the dihedral angle between the particles size and the sintering force is shown by the star-shaped symbols marked in the figure. The sintering force is approximately 0.42×10^{-6} N for a particle radius of 2 μm, a neck radius of 0.5 μm, and a dihedral angle of 135°, while sintering force is extremely small when the particle and neck radii are both 2 μm, and a dihedral angle approximately equal to 180°.

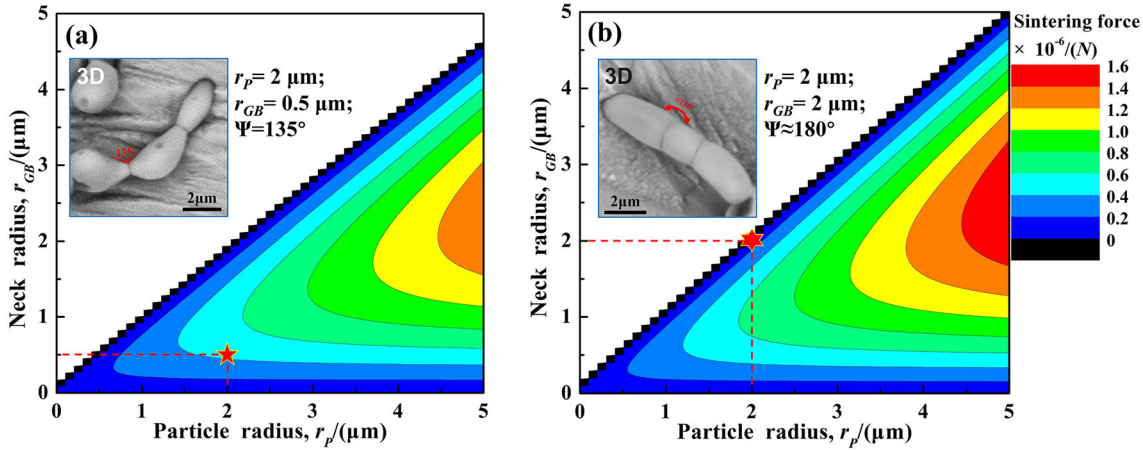

Fig. 6. Sintering force as a function of particle and neck radius: (a) ψ = 135°; (b) ψ = 180°.

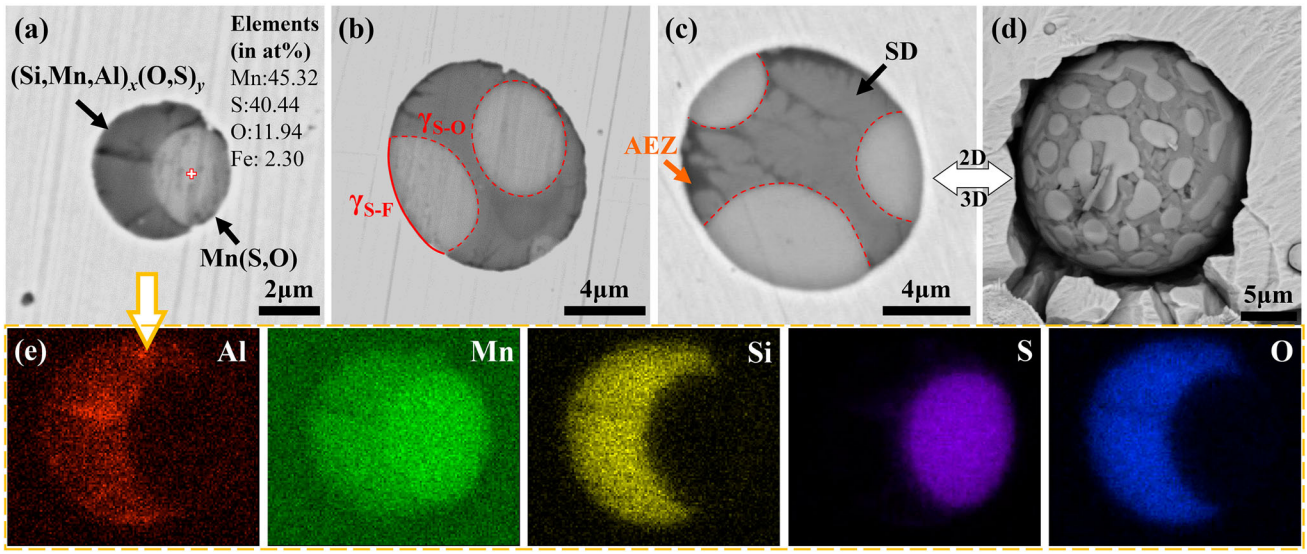

Fig. 7. Oxysulfide-oxide composite inclusions (Si,Mn,Al)$_x$(O,S)$_y$: (a) to (c) 2D morphology; (d) 3D morphology; (e) element mapping for the inclusion in (a) (Color figure online).

Composite Inclusion Mn(S,O)-MO$_{x(M = Si,Al,Mn,Fe)}$

Since oxygen content in free-cutting steels is used to modify the morphology of sulfide and the machinability of steel, the oxides are by-products formed by oxygen and deoxidizer in steel during solidification process. In 1215MS free-cutting steel, oxide-oxysulfide composite inclusions with different sizes and compositions were found; their size ranges from a few micrometers to > 10 μm, as shown in Fig. 7. Oxysulfide-oxide composite inclusions are almost all spherical or ellipsoidal in shape with diameters ranging from 5 μm to 20 μm, as shown in Fig. 7a–d. The area of oxide takes the dominate role in the composite inclusions, while the area of sulfides is low. The EDS result shows that the oxygen content in oxysulfide part of the composite inclusion in Fig. 7a is lower than that in single-particle oxysulfide. The precipitation of oxide-sulfide composite inclusions is extremely complex. It depends on the mass percent of oxide or sulfide that takes the dominating role. Gleinig[25] suggested that the liquid oxide first nucleated and precipitated, after which the sulfide formed embryos on the surface of liquid oxide inclusions, and then sulfide embryos further nucleated and grew. However, according to the 2D morphology of the composite inclusions in 1215MS free-cutting steel observed by SEM, sulfide is not exactly at the periphery of oxide but forms a whole spherical inclusion with oxide. This means that in either oxide first nucleation or sulfide first nucleation, they are a complete sphere, i.e., they are liquid (Si,Mn,M)$_x$(O,S)$_y$ inclusions at high temperature; M is the possible alloying element, such as Al and Fe.

Kim et al.[26] suggested that Mn and S are continuously transferred from the steel to the solid

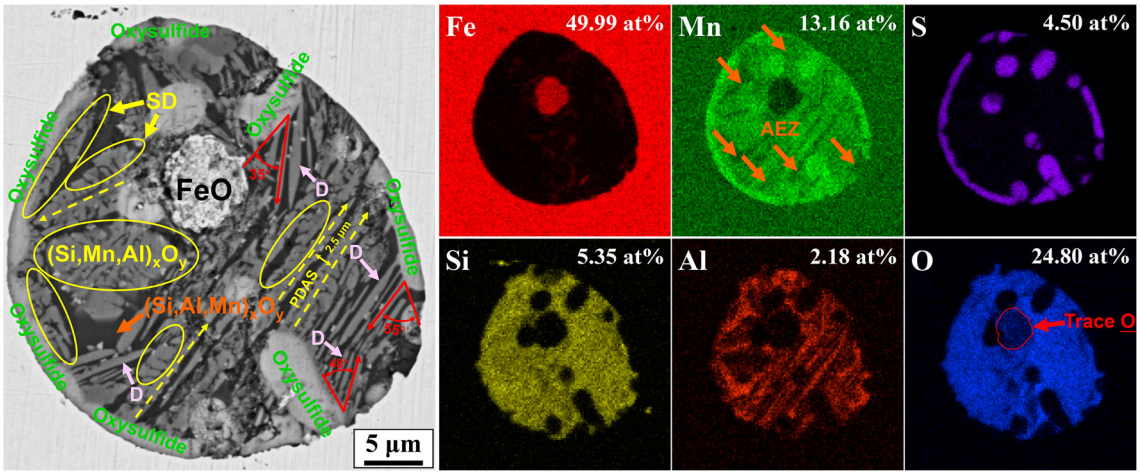

Fig. 8. Final morphology and element mapping of liquid inclusion $(Mn,Si,Al,Fe)_x(O,S)_y$ (Color figure online).

silicon-manganese oxide surface and form liquid MnS, while Zhang et al.[12] concluded that the temperature of liquid $(Mn,Si)_x(S,O)_y$ inclusions in silicon deoxidized free-cutting steels is 1250°C. They all believed that liquid inclusion is the important part of composite inclusion. The phase diagram of $MnO\text{-}SiO_2\text{-}Al_2O_3$ system shows that the melting point of $MnO\text{-}SiO_2\text{-}Al_2O_3$ inclusion is < 1200°C.[27] Therefore, due to the similarity of their melting points, the precipitation orders of $(Si,Mn,Al)_x(O,S)_y$ and Mn(S,O) can be discussed according to the their morphologies in Fig. 7b and c. The melting points of both $(Si,Mn,Al)_x(O,S)_y$ and Mn(S,O) are lower than the solidus temperature of steel, combining the smaller interface curvature between oxysulfide and steel rather than between oxysulfide and oxide. It can be concluded that the interfacial energy of oxysulfide and steel, $\gamma_{S\text{-}F}$ (as shown the red line in Fig. 7b), is bigger than that of oxysulfide and oxide, $\gamma_{S\text{-}O}$ (as shown the red dashed line in Fig. 7b and c). According to the morphology of $(Si,Mn,Al)_x(O,S)_y$, it looks like the seaweed dendrite (SD) precipitated on Mn(S,O) substrate, which means oxysulfide is precipitated before oxide.

There is a dark zone between SD and Mn(S,O) substrate. It is confirmed to be the aluminum-enriched zone (AEZ) based on the morphology of complex composite inclusion, $(Mn,Si,Al,Fe)_x(O,S)_y$, as shown in Fig. 8. According to the results of the element mapping of this inclusion, the main composition of the inclusions can be divided into $(Si,Mn,Al)_xO_y$, $(Si,Al,Mn)_xO_y$, MnS and FeO, and their area ratio decreases in order. The difference between $(Si,Mn,Al)_xO_y$ and $(Si,Al,Mn)_xO_y$ is their element content of Al and Mn. $(Si,Mn,Al)_xO_y$ is the silicon-manganese oxide with trace Al, while the content of Mn is less than that of Al in $(Si,Al,Mn)_xO_y$.

The element mapping for Fe contains a small amount of O element, which indicates that what is formed is FeO. Generally, the formation Gibbs free energy of the liquid (FeO and MnS) is lower than that of the solid.[28,29] Therefore, their formation Gibbs free energies were compared to analyze the precipitation order in the composite inclusion in Fig. 8. The standard free energy of liquid ferrous oxide formation can be expressed as.[28]

$$\Delta G^{\theta}_{FeO(l)} = -109467 + 45.647\,T \quad (J/mol) \qquad (4)$$

The standard Gibbs free energy of liquid MnS is:[29]

$$\Delta G^{\theta}_{MnS(l)} = -140465 + 79.68\,T \quad (J/mol) \qquad (5)$$

The critical temperature for the formation of liquid phase ferrous oxide (2125.49°C, 2398.49 K) is much higher than that of liquid phase sulfide (1489.86°C, 1762.86 K), which indicates that FeO can precipitate before sulfide at the same temperature. According to the morphology of $(Si,Mn,Al)_xO_y$ on the left side of FeO, the $(Si,Mn,Al)_xO_y$ near the FeO end grows to the right, and the length of the primary dendrite (as shown by the yellow dashed line) is approximately 15 μm. The end of the primary dendrite is close to the oxysulfide substrate, while the oxysulfide induces the precipitation of SD $(Si,Mn,Al)_xO_y$ (as shown by the yellow circle) from the other side. The liquid oxysulfide completely wetted on the oxide surface is first transformed into solid during solidification, which acts as a heterogeneous nucleus for $(Si,Mn,Al)_xO_y$, so that $(Si,Mn,Al)_xO_y$ forms two shapes, the SD and the dendrite (D). It can grow with Mn(S,O) as the substrate and also form secondary dendrites perpendicular to the primary dendrite. The primary dendrite arm space (PDAS) is approximately 2.5 μm. The angle between D and oxysulfide substrate is in a range from 35° to 78° (red angle), as shown by the pink arrows. The dendrites without secondary dendrite indicate a good growth orientation relationship for the growth of $(Si,Mn,Al)_xO_y$ on sulfide.[30,31] According to the results of the element mapping of Mn, the area

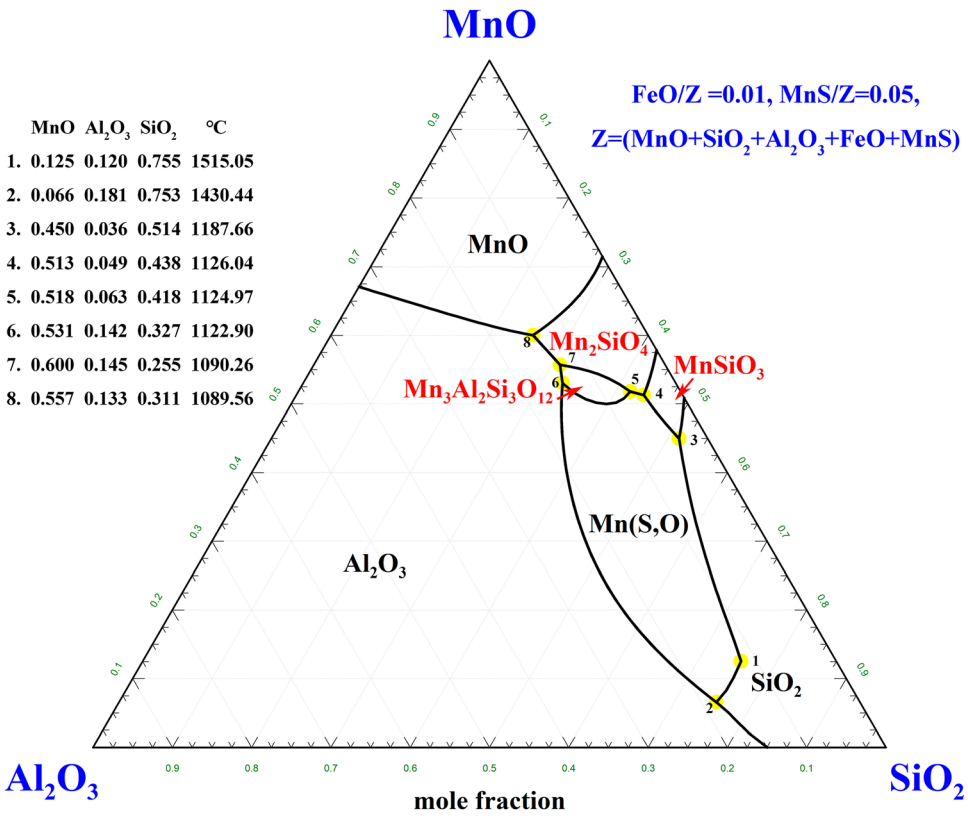

Fig. 9. Projection phase diagram of different predominant phases in the liquid phase.

indicated by the orange arrow in the figure is AEZ, which indicates that with the reaction of Mn with sulfur and oxygen, the remaining Si, Al and a small amount of Mn form the liquid $(Si,Al,Mn)_xO_y$ with lower melting point part with oxygen content. It shows no feature of morphology, with filling the voids between other phases, indicating that it is a solvent for the formation of other phases, and its melting point is lower than that of $(Si,Mn,Al)_xO_y$.

Therefore, based on the morphology and thermodynamics analysis of $(Mn,Si,Al,Fe)_x(O,S)_y$, the elemental partition present in $(Mn,Si,Al,Fe)_x(O,S)_y$ leads to a different precipitation order of the components. The liquid inclusions are precipitated in the following order: FeO, MnS, $(Si,Mn,Al)_xO_y$ and $(Si,Al,Mn)_xO_y$. Projection phase diagrams of different phases in the liquid phase have been calculated via Factsage 7.3 when FeO and MnS were set as 1 at.% and 5 at.%, respectively; the result is shown in Fig. 9. Eight phase transition points have been marked, and the lines they formed reflect the trend of phase transition with temperature changes. Oxysulfide precipitates first. With decreasing temperature, oxide forms as $MnSiO_3$, and Mn_2SiO_4 is formed when the oxygen content in the $MnO\text{-}SiO_2$ system is sufficient.[32] When the atomic content of Al_2O_3 is < 0.063, $(Si,Mn,Al)_xO_y$ is considered to be Mn_2SiO_4 with Al. With increasing Al_2O_3 content, the melting point of $(Si,Al,Mn)_xO_y$ keeps decreasing from 1124.97°C to 1090.26°C, as line 57 in Fig. 9; when it is > 0.063, $(Si,Al,Mn)_xO_y$ might be $Mn_3Al_2Si_3O_{12}$ according to the projection phase diagram.

In summary, the composite inclusion $Mn(S,O)\text{-}MO_{x(M\ =\ Si,Al,Mn,Fe)}$ is formed by FeO, Mn(S,O), $(Si,Mn,Al)_xO_y$ and $(Si,Al,Mn)_xO_y$ in precipitation order. The content of Al_2O_3 has a crucial impact on the precipitation type of complex oxides. The liquid inclusion undergoes the following phase change process:

$$\begin{aligned}(\mathrm{Mn,Si,Al,Fe})_x(\mathrm{O,S})_y(\mathrm{l}) &\rightarrow \mathrm{FeO} \\ &+ (\mathrm{Mn,Si,Al})_x(\mathrm{O,S})_y \rightarrow \mathrm{FeO} + \mathrm{Mn(S,O)} \\ &+ (\mathrm{Si,Mn,Al})_x(\mathrm{O,S})_y \rightarrow \mathrm{FeO} + \mathrm{Mn(S,O)} \\ &+ (\mathrm{Si,Mn,Al})_x\mathrm{O}_y + (\mathrm{Si,Al,Mn})_x\mathrm{O}_y\end{aligned}$$

CONCLUSION

Based on the theoretical and experimental analysis, the formation mechanisms of four typical sulfides in 1215MS free-cutting steel with 50 ppm oxygen content have been analyzed; the main conclusions can be summarized as follows:

1. The liquidus and solidus temperatures of the steel are 1512.92°C and 1458.79°C, and the precipitation temperature of sulfide in steel at equilibrium state is 1489.98°C, while oxygen can

dissolve in sulfide to form single-particle spherical Mn(S,O) containing 19 at.% oxygen with a melting point of approximately 1188°C.

2. Annular polycrystalline Mn(S,O) with a diameter of 10 μm is formed after three evolution stages: contact, sintering and densification. Sintering force is a vital force in the formation of polycrystalline Mn(S,O); when the particle and the neck radii are 2 μm and 0.5 μm, respectively, the sintering force is approximately 0.42×10^{-6} N under a dihedral angle of 135°, while it is extremely small when the particle and neck radii are similar in the later stage of sintering.
3. Complex composite inclusion is formed by a liquid inclusion that undergoes the following phase change process:

$$\begin{aligned}(\mathrm{Mn,Si,Al,Fe})_x(\mathrm{O,S})_y(\mathrm{l}) &\rightarrow \mathrm{FeO} \\ &+ (\mathrm{Mn,Si,Al})_x(\mathrm{O,S})_y \rightarrow \mathrm{FeO} + \mathrm{Mn(S,O)} \\ &+ (\mathrm{Si,Mn,Al})_x(\mathrm{O,S})_y \rightarrow \mathrm{FeO} + \mathrm{Mn(S,O)} \\ &+ (\mathrm{Si,Mn,Al})_x\mathrm{O}_y + (\mathrm{Si,Al,Mn})_x\mathrm{O}_y\end{aligned}$$

The atomic content of Al_2O_3 in liquid inclusion has a crucial impact on the precipitation types of oxides. When it is < 0.063, $(Si,Mn,Al)_xO_y$ is Mn_2SiO_4 with dissolved Al. With increasing content of Al_2O_3, the melting point of $(Si,Al,Mn)_xO_y$ keeps decreasing from 1124.97°C to 1090.26°C; when it greater than 0.063, $(Si,Al,Mn)_xO_y$ is $Mn_3Al_2Si_3O_{12}$.

ACKNOWLEDGEMENTS

The authors express their appreciation to National Natural Science Foundation of China (Grant No. 52074179) for supporting this work. One of the authors, Xiangyu Xu, gratefully acknowledges support from the National Natural Science Foundation of China (Youth Program no. 52104335) and Shanghai "Super Postdoctoral" Incentive Plan (Grant No. 2020194).

CONFLICT OF INTEREST

The authors declare that they have no conflict of interest.

REFERENCES

1. Y. Wang, Y. Yang, Z. Dong, J.H. Park, Z. Mi, X. Mao, and W. Mu, *Metall. Mater. Trans. B* 53, 2182 (2022).
2. L. Jin, S. Zheng, and M. Zhu, *JOM* (2023), published online.
3. C. Temmel, B. Karlsson, and N. Ingesten, *Metall. and Mater. Trans. A* 37, 2995 (2006).
4. L.E.K. Holappa, and A.S. Helle, *J. Mater. Process. Tech.* 53, 177 (1995).
5. N. Tsunekage, and H. Tsubakino, *ISIJ Int.* 41, 498 (2001).
6. T. Nishimura, S. Koishi, Y. Yamamoto, Y. Wada, K. Mine, and Y. Shinjo, *Kawasaki Steel. Tech. Rep.* 8, 77 (1983).
7. C.E. Sims, *Trans. Am. Inst. Min. Metall. Eng.* 215, 367 (1959).
8. S. Lin, H. Yang, Y. Su, K. Chang, C. Yang, S. Lin, and J. Alloy, *Compd.* 779, 844 (2019).
9. D.H. Woo, H.G. Lee, and J. Am, *Ceram. Soc.* 93, 2098 (2010).
10. Y.J. Kim, D.H. Woo, H. Gaye, H. Lee, and T. Kang, *Metall. Mater. Trans. B* 42, 535 (2011).
11. G. Wang, S. Li, X. Ai, C. Zhang, and C. Lai, *J. Iron Steel Res. Int.* 22, 566 (2015).
12. Q. Zhang, Y. Min, H. Xu, and C. Liu, *ISIJ Int.* 58, 1250 (2018).
13. Y. Ren, and L. Zhang, *Ironmak. Steelmak.* 46, 558 (2019).
14. Q. Tian, B. Liu, W. Shen, T. Hu, J. Fu, and X. Xu, *Steel Res. Int.* 4, 2200674 (2023).
15. E.T. Turkdogan, G.J.W. Kor, L.S. Darken, and R.W. Gurry, *Metall. Trans.* 2, 1561 (1971).
16. G.J.W. Kor, and E.T. Turkdogan, *Metall. Trans.* 3, 1269 (1972).
17. M. Nakamoto, T. Tanaka, M. Suzuki, K. Taguchi, Y. Tsukaguchi, and T. Yamamoto, *ISIJ Int.* 54, 1195 (2014).
18. S. Lee, and W.M. Sigmund, *Colloid. Surface. A* 204, 43 (2002).
19. W.Z. Mu, N. Dogan, and K.S. Coley, *Metall. Mater. Trans. B* 48, 2092 (2017).
20. W.Z. Mu, N. Dogan, and K.S. Coley, *Metall. Mater. Trans. B* 48, 2379 (2017).
21. O. Sudre, and F.F. Lange, *J. Am. Ceram. Soc.* 75, 3241 (1992).
22. D.A. Caillet, and D.P. Harrison, *Chem. Eng. Sci.* 37, 625 (1982).
23. F. Wakai, K. Katsura, S. Kanchika, Y. Shinoda, T. Akatsu, and K. Shinagawa, *Acta Mater.* 109, 292 (2016).
24. F. Wakai, and K.A. Brakke, *Acta Mater.* 59, 5379 (2011).
25. J. Gleinig, A. Weidner, J. Fruhstorfer, C.G. Aneziris, O. Volkova, and H. Biermann, *Metall. Mater. Trans. B* 50, 337 (2019).
26. H.S. Kim, H.G. Lee, and K.S. Oh, *Metall. Mater. Trans. A* 32, 1519 (2001).
27. J. Chen, Q. Zhu, D. Huang, S. Zheng, J. Zhang, and H. Li, IOP Conference Series: Mater. *Sci. Eng.* 230, 012030 (2017).
28. M. Wakoh, T. Sawai, and S. Mizoguchi, *Tetsu-to-Hagané* 78, 1697 (1992).
29. Y. Lu, and T. Miki, *ISIJ Int.* 61, 2360 (2021).
30. P.N. Quested, and M. McLean, *Mater. Sci. Eng.* 65, 171 (1984).
31. S. Akamatsu, and G. Faivre, *Phys. Rev. E* 58, 3302 (1998).
32. Y. Kurosaki, M. Shiozaki, K. Higashine, and M. Sumimoto, *ISIJ Int.* 39, 607 (1999).